International Communications in Heat and Mass Transfer 179 (2026) 112238

Contents lists available at ScienceDirect

International Communications in Heat and Mass Transfer

journal homepage: www.elsevier.com/locate/ichmt

Visualization of imbibition front stability in hybrid wire-mesh media with grooved structures

Jian Tian [a,b], Yugao Ma [c,*], Haonan Hou [a,b], Suyi Zhang [c], Chaozhong Qin [a,b,**]

[a] State Key Laboratory of Coal Mine Disaster Dynamics and Control, Chongqing University, Chongqing, China
[b] School of Resources and Safety Engineering, Chongqing University, Chongqing, China
[c] Nuclear Power Institute of China, China

ARTICLE INFO

Keywords:
Hybrid porous media
Wicking structures
Metal wire mesh
Interfacial instability
Horizontal imbibition

ABSTRACT

Hybrid porous media spontaneous imbibition is governed by coupled capillary force and flow resistance. Grooved metal mesh wicks reduce flow resistance and boost permeability, but existing studies only discuss overall imbibition acceleration, lacking systematic clarification on cross-scale liquid exchange between macro-grooves and micro-mesh, and quantitative laws of imbibition front instability. This study reports a systematic investigation combining high-resolution visualization and theoretical analysis to clarify the regulatory effects of grooved structures on horizontal imbibition dynamics. In contrast to the uniform piston-like displacement in plain meshes, the incorporation of grooves generates a lateral capillary pressure gradient, triggering non-uniform fingering instability across the global front. This phenomenon originates from a transverse liquid supply mechanism, in which grooves replenish adjacent mesh regions. Quantitative analysis based on Chuoke's theory reveals a critical trade-off: grooves significantly enhance working fluid imbibition rate in adjacent mesh regions but destabilize the overall imbibition front. Among all geometric variables, groove quantity dominates imbibition performance regulation, exerting a much more pronounced influence on liquid uptake speed than groove cross-sectional dimension. The results provide physical design criteria for composite grooved mesh wicks, guiding thermal and energy equipment requiring rapid liquid transport and stable flat imbibition fronts, such as heat pipes and fuel cell gas diffusion layers (GDL).

1. Introduction

Spontaneous imbibition refers to the physical phenomenon whereby a wetting fluid is spontaneously drawn into porous media by capillary pressure, displacing the non-wetting fluid [1]. This capillary-governed transport widely occurs across energy engineering, thermal management, environmental remediation and plant physiological processes [2–6], forming a core transport mechanism that determines the efficiency of many industrial and natural systems. Comprehensive understanding of imbibition kinetics and interfacial evolution is therefore essential for both fundamental two-phase flow theory and practical process optimization.

Metal wire mesh stands out as a favorable experimental medium for capillary flow research, owing to its uniform, precisely tunable pore geometry and easy fabrication; it also serves as a core wick component for heat pipes [7]. Traditional mesh optimization strategies rely solely on adjusting mesh count and weave patterns to balance capillary suction and liquid transport capacity [8–10]. Nevertheless, single-scale mesh structures suffer rapidly rising flow resistance with extended imbibition distance, which drastically suppresses liquid uptake speed. To mitigate this limitation, researchers have introduced macroscopic grooves into homogeneous meshes to construct dual-scale composite porous media, which deliver mass transfer improvements unattainable with single-pore structures [11–14]. Fabricated via stamping, laser etching or electrochemical machining, grooves feature far larger cross-sections than native mesh pores and act as low-resistance liquid flow channels. Such structures are widely adopted in heat pipe wicks and fuel cell flow plates to facilitate uniform fluid distribution, making them a mainstream composite medium design route [15–17]. However, the cross-scale mass exchange between grooves and adjacent mesh regions, and its effect on imbibition front stability remain unclear.

A body of existing research has examined imbibition performance in

* Corresponding author at: Nuclear Power Institute of China, China.
** Corresponding author at: State Key Laboratory of Coal Mine Disaster Dynamics and Control, Chongqing University, Chongqing, China.
E-mail addresses: mayugao@npic.ac.cn (Y. Ma), chaozhong.qin@cqu.edu.cn (C. Qin).

https://doi.org/10.1016/j.icheatmasstransfer.2026.112238

Available online 1 August 2026

grooved mesh composites, laying a foundational framework for this field. Khrustalev et al. built an early heat transfer model for mesh-microgroove assemblies and clarified the coupling between capillary pressure and flow resistance [18]. Ravi et al. experimentally verified that composite structures combine the high capillary force of meshes and low flow resistance of grooves to achieve superior imbibition capacity compared with single components [19]. Visualization tests by Jiang et al. further confirmed that groove wall micro-morphology alters dynamic wetting and the uneven propagation of imbibition fronts [20]. Complementary analytical models developed by Wong et al. quantified how structural parameters govern lateral liquid supply, supporting parametric wick design [21]. Laser-fabricated variable-aspect-ratio microgrooves tested by Liu et al. demonstrated that optimized groove geometry can significantly reduce heat pipe thermal resistance [22].

Despite revealing basic flow features of grooved composite meshes, existing research has three key limitations motivating this work: (1) Most studies only characterize overall permeability and imbibition acceleration, ignoring cross-scale mass exchange between grooves and meshes [23]; (2) Few systematically correlate groove geometry (size and number) with lateral liquid supply [24]; (3) Traditional theories treat composite media as homogeneous continua and neglect local cross-scale capillary flow differences, failing to explain irregular unstable imbibition front evolution [24,25]. These unresolved gaps highlight the need for integrated visual and theoretical analysis to unpack the coupled effects of groove structures on horizontal imbibition dynamics.

This work adopts regular wire mesh samples with pressed semi-circular grooves and combines high spatiotemporal resolution visualization with capillary pressure-based instability theory to systematically reveal how groove geometry regulates imbibition front evolution and liquid uptake rate. The innovative contributions of this work are summarized: (1) direct visual evidence of the dual competing effect of grooves—they accelerate mesh-region imbibition while triggering interfacial instability; (2) a mechanistic explanation of lateral liquid supply built upon Chuoke's two-phase interfacial instability criterion [26]; (3) quantitative differentiation of groove number as the dominant controlling factor over groove size. The outcomes advance fundamental theory for spontaneous imbibition in dual-scale composite porous media, provide parametric design guidance for wick structures in heat pipes and fuel cell gas diffusion layers, and offer repeatable experimental and analytical frameworks for future related capillary flow research.

2. Materials and methods

2.1. Experimental set-up

As illustrated in Fig. 1, the experimental set-up comprises a custom-fabricated specimen holder for horizontal imbibition tests, manufactured via 3D printing to eliminate gravitational effects on imbibition front evolution and working fluid dynamic distribution. The specimen holder is composed of two main functional zones. On the left, a reservoir for storing and continuously supplying the working fluid to the wire mesh specimen. On the right, a specimen chamber for holding the wire mesh specimen. The overall external dimensions of the specimen holder are 170 mm (length) × 60 mm (width) × 20 mm (height), while the reservoir measures 50 mm (length) × 50 mm (width) × 15 mm (height). A high-definition camera was used to record the imbibition process in real time at a frame rate of 30 fps.

2.2. Materials

A 400-mesh metal wire mesh was used as the base material. The measured wire diameter was 29 μm, the pore size was 33 μm, and the thickness was approximately 60 μm. The basic parameters of the wire

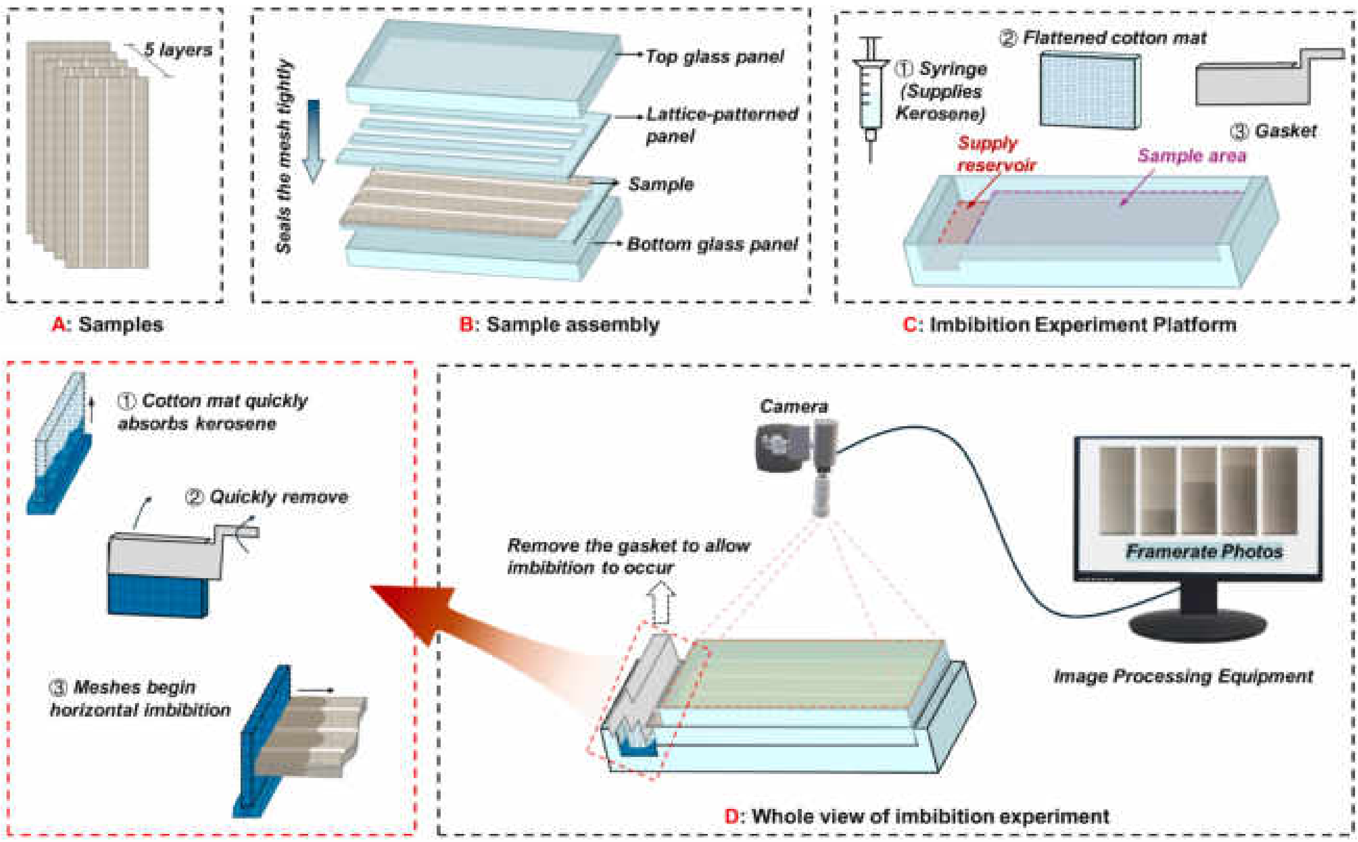

Fig. 1. Schematic diagram of the experimental setup and procedure.

mesh are listed in Table 1. As shown in Fig. 2, several standard specimens measuring 10 cm in length and 4 cm in width were made from the wire mesh using laser cutting. Subsequently, grooves with a semicircular cross-section were embossed onto the surface of the standard specimens by a stamping process. The groove diameters were fabricated as 1.0 mm, 1.5 mm, and 2.0 mm, respectively, and the number of grooves was designed as 1 or 3. All grooves were equally spaced along the width direction of the specimens. Finally, specimens with intact grooved structures and flat mesh surfaces were selected for the imbibition experiments. Prior to testing, the wire mesh substrate was confirmed to possess favorable oleophilicity; thus, kerosene was selected as the working fluid for imbibition experiments.

2.3. Experimental methods

As a control group, five standard wire mesh specimens without grooved structures were stacked and aligned vertically for horizontal imbibition experiments. To investigate the effect of the grooved structures, imbibition experiments were conducted on a stack consisting of three wire mesh specimens with grooved structures and two wire mesh specimens without grooved structures, with the bottom two layers being the specimens without grooves and the top three layers being the specimens with grooves (Fig. 1-A). To prevent deformation or damage to the grooved structures during imbibition, a protective plate matching the dimensions and layout of the grooves was fabricated, with hollowed-out features at the corresponding positions to accommodate the grooves (Fig. 1-B). To avoid additional imbibition of kerosene through the gaps between the wire mesh specimens and the protective plate, the plate was made of polytetrafluoroethylene (PTFE), which is oleophobic. All experiments were conducted at a room temperature of 21 °C and the main experimental procedures were as follows:

a) The assembled wire mesh wick specimen was placed in the specimen holder. A piece of tempered glass was then placed on top of the specimen to fix and compact it, ensuring that the spacing between wire mesh layers remained consistent each time the specimen was replaced (Fig. 1-C). The imaging system was then turned on, and the working distance, magnification, and position of the specimen holder were adjusted until a clear image of the specimen was obtained in the acquisition software.
b) Video recording was started in advance to capture the spontaneous imbibition process of the working fluid in the wire mesh wick specimen in real time, and the spatiotemporal evolution of the imbibition front was observed.
c) Kerosene was slowly injected into the reservoir using a syringe until the cotton mat was completely wetted. The blocking spacer (which prevented premature contact of the working fluid with the specimen) was then quickly removed, allowing kerosene to contact the specimen through the cotton mat at the cross-sectional end, thereby triggering the horizontal imbibition process (Fig. 1-D).
d) The experiment was terminated when the wire mesh wick with grooves was completely wetted or when the imbibition front showed no significant change within 3 min. The video data were saved for subsequent analysis.
e) The wire mesh wick specimen was replaced with one having a different grooved Structure, and steps (a) through (d) were repeated until all specimens had been tested.

Table 1
The basic parameters of the metal mesh specimen.

Mesh count	Aperture, μm	Wire diameter, μm	Thickness, μm
400	33	29	60

3. Results

3.1. Front evolution in plain wire mesh

Based on the real-time video data recorded by a high-definition camera, the spontaneous imbibition process of the metal wire mesh without grooved structures was quantified. Since the total effective length of the wire mesh specimen was 10 cm, whenever the imbibition front advanced by 1 cm during the spontaneous imbibition process, a key frame image at the corresponding moment was extracted from the video as a result. In this way, the complete evolution of the advancing distance of interface front from 0 cm to 10 cm during imbibition was obtained. Fig. 3 shows the whole evolution process of interface front. The numbers at the top of the figure indicate the advancing distance of the imbibition front (L, in cm), while the numbers at the bottom indicate the imbibition time (t, in s) at each position. Experimental results indicate that for the groove-free wire mesh specimen, the imbibition front during spontaneous imbibition displays stable, piston-like, one-dimensional propagation. The entire imbibition front remains relatively horizontal throughout the process, without obvious fluctuations or deformations.

3.2. Front evolution in grooved wire mesh

Using the same image processing method as described in the preceding experiments, the evolution images of the spontaneous imbibition process were obtained for wire mesh specimens containing different grooved structures, as shown in Figs. 4, 5, and 6, respectively. The experimental results show that adding grooves to the wire mesh causes kerosene imbibition to develop distinct non-uniform fingering phenomenon, in stark contrast to the uniform piston-like advancement shown in Fig. 3. Comparison of the experimental results for grooved structures with different groove numbers (Figs. 4, 5, and 6) indicates that the morphological evolution of the imbibition front is closely related to the number of grooves. Specifically, when a single groove is present, the imbibition front of kerosene in the wire mesh regions on both sides of the groove still maintains a uniform piston-like advancement. However, when the number of grooves increases to three, the fingering phenomenon at the imbibition front becomes increasingly pronounced, and the advancement velocity of the imbibition front in the wire mesh regions is significantly faster than that inside the grooves. These findings demonstrate that the introduction of grooved structures significantly affects both the advancement velocity and the interfacial stability of the imbibition front, with the number of grooves playing a more pronounced role than groove size.

For specimens with a single groove, regardless of groove diameter (1.0 mm, 1.5 mm, or 2.0 mm), the imbibition front in the wire mesh regions on both sides consistently maintains a stable, piston-like advancement (Figs. 4, 5, and 6, top row). In contrast, when the groove number increases to three, pronounced non-uniform fingering emerges. Notably, the fingering intensity becomes increasingly severe with larger groove diameters: the 2.0 mm triple-groove specimen exhibits the most distorted interface, while the 1.0 mm triple-groove specimen shows relatively milder but still significant front instability (Figs. 4, 5, and 6, bottom row). These observations demonstrate that while a single groove does not disturb front stability regardless of its size, multiple grooves synergize with increased diameter to amplify interfacial deformation.

4. Discussion

4.1. Validation of the Lucas-Washburn model

When gravitational effects are neglected, the spontaneous imbibition process in homogeneous porous media follows the classical Lucas-Washburn (L-W) model, which describes a linear relationship between the imbibition distance and the square root of time [27,28]. To validate

Fig. 2. Images of the wire mesh used in this work. (a) Standard specimen with 10 cm in length and 4 cm in width. (b) specimens with 1 groove and 3 grooves of 2 mm in size. (c) The cross-sectional structure of a 2 mm groove.

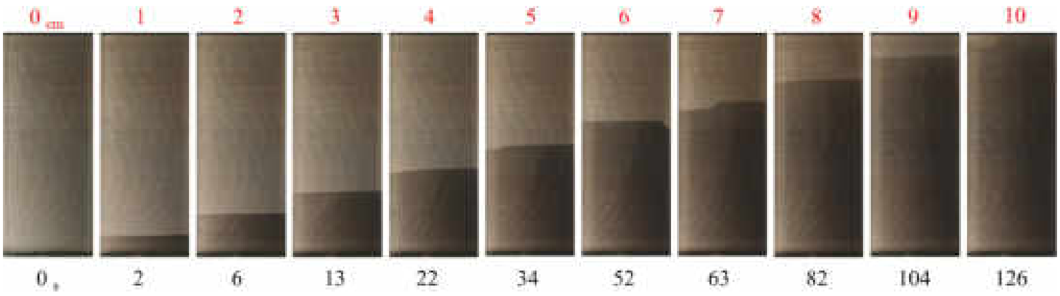

Fig. 3. Real-time evolution of the interface front during horizontal imbibition of the wire mesh without grooves. The red numbers indicate the propagation distance of the front (cm), and the black numbers indicate the corresponding time at each distance (s). (For interpretation of the references to colour in this figure legend, the reader is referred to the web version of this article.)

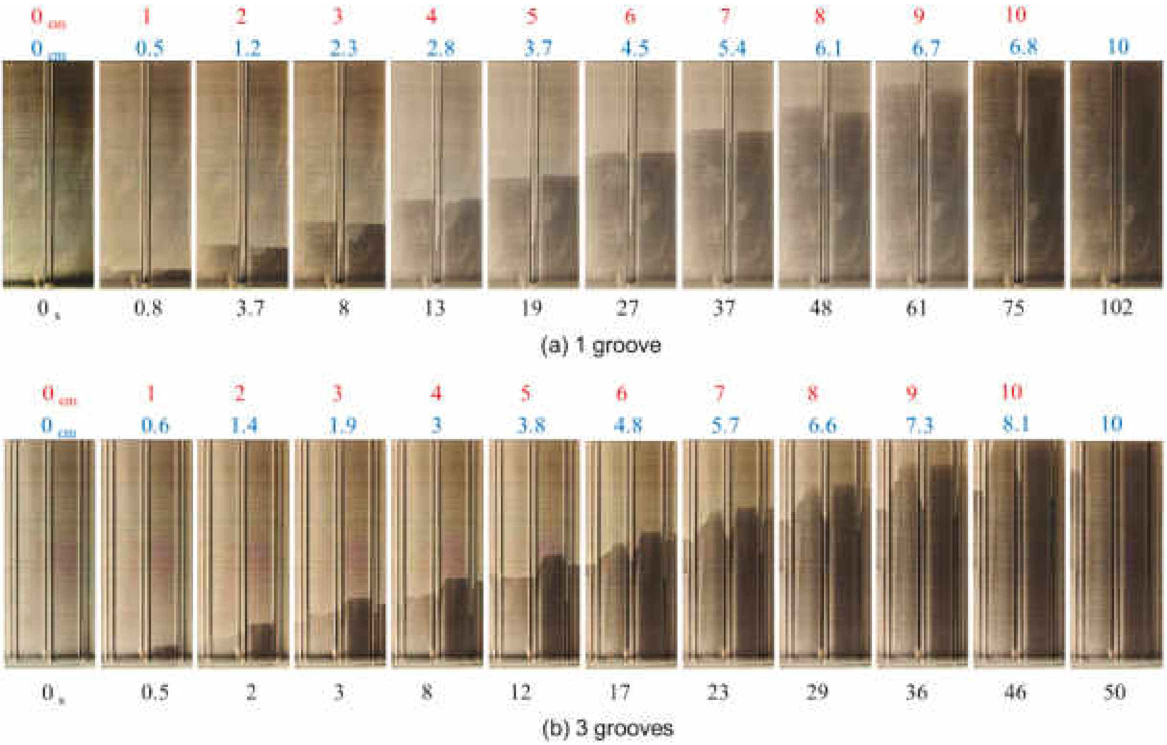

Fig. 4. Real-time evolution of the interface front during horizontal imbibition of the wire mesh with grooves of 1 mm diameter and varying groove numbers. The red numbers indicate the maximum advancement distance of the imbibition front evolution in the wire mesh regions. The blue numbers indicate the minimum advancement distance of the imbibition front evolution in the groove regions. The black numbers indicate the corresponding time at each distance (s). (For interpretation of the references to colour in this figure legend, the reader is referred to the web version of this article.)

whether the horizontal spontaneous imbibition process conforms to the classical *L*-*W* capillary imbibition model, the relationship curves between the imbibition front advancing distance (*L*, in cm) and the imbibition time (*t*, in s), as well as between *L* and the square root of time $t^{0.5}$, were plotted based on the experimental results of the wire mesh specimen without grooved structures presented in Section 3.1. Neglecting the effects of gravity and inertial forces, the theoretical prediction formula of the *L*-*W* imbibition length model for porous media under the

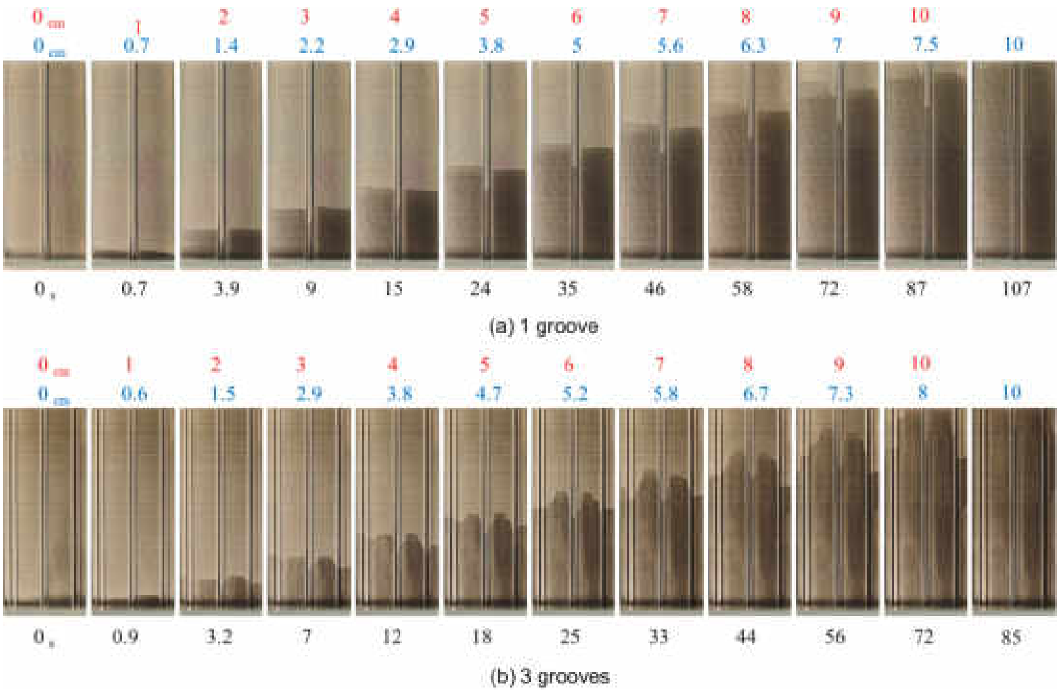

Fig. 5. Real-time evolution of the interface front during horizontal imbibition of the wire mesh with grooves of 1.5 mm diameter and varying groove numbers. The red numbers indicate the maximum advancement distance of the imbibition front evolution in the wire mesh regions. The blue numbers indicate the minimum advancement distance of the imbibition front evolution in the groove regions. The black numbers indicate the corresponding time at each distance (s). (For interpretation of the references to colour in this figure legend, the reader is referred to the web version of this article.)

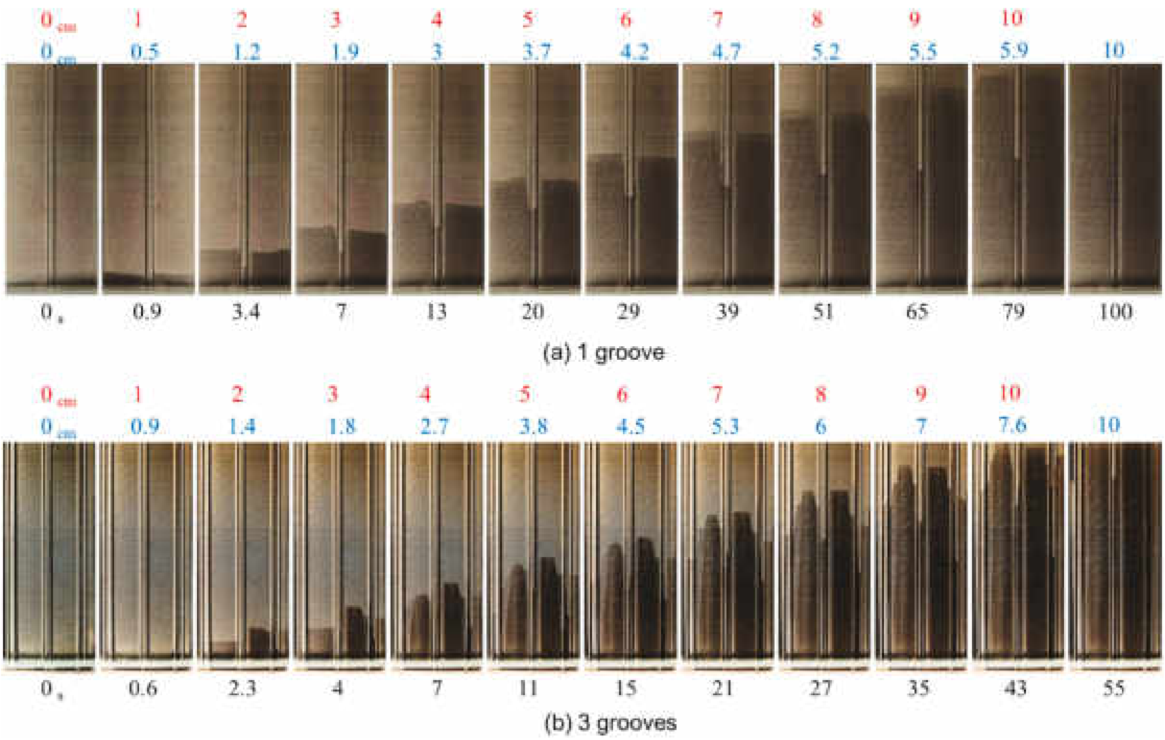

Fig. 6. Real-time evolution of the interface front during horizontal imbibition of the wire mesh with grooves of 2 mm diameter and varying groove numbers. The red numbers indicate the maximum advancement distance of the imbibition front evolution in the wire mesh regions. The blue numbers indicate the minimum advancement distance of the imbibition front evolution in the groove regions. The black numbers indicate the corresponding time at each distance (s). (For interpretation of the references to colour in this figure legend, the reader is referred to the web version of this article.)

horizontal spontaneous imbibition condition investigated in this study is expressed as [29]:

$$L = \sqrt{\frac{r\sigma cos\theta}{2\mu\tau^2}t} \quad (1)$$

where L denotes the imbibition length of the working fluid inside the wire mesh, r represents the equivalent capillary radius of the wire mesh, σ is the interfacial tension between the imbibition working fluid and air, θ is the contact angle of the imbibition working fluid, μ refers to the dynamic viscosity of the imbibition working fluid, and τ is the tortuosity of the wire mesh specimen. The imbibition working fluid used in this experiment is industrial kerosene, the experimental temperature is room temperature of 21 °C, and the mesh number of the metal wire screen is 400. The relevant parameter values under the experimental conditions in this study obtained by literature are listed in Table 2. Based on the geometric parameters of the 400-mesh twill-weave wire screen (d = 29 μm, a = 33 μm), the tortuosity is theoretically estimated to be in the range of 1.45–1.55 for a single layer and 1.60–1.72 for five stacked layers [29]. Therefore, the τ will be taken as 1.5, 1.6, and 1.7 for the *L-W* model calculation in our study, respectively.

Based on the above L-W imbibition theoretical model and the parameters listed in Table 2, the comparison between the theoretically predicted imbibition curves of metal wire mesh and the experimentally fitted imbibition curves is presented in Fig. 7. It can be observed that the experimental data show good consistency with the trend predicted by the theoretical model. In particular, when the τ is set to 1.6, the experimental data are basically in agreement with the theoretical predictions, which verifies that the experimental results of this study conform to the *L-W* prediction model.

4.2. Effect of grooves on imbibition front morphology

Mesh samples free of grooves were selected as the benchmark in this study. The spatial coordinates of the imbibition front at different time points were extracted to plot the spatial evolution profile of the imbibition front, so as to analyze the influence of grooves on imbibition front stability. The detailed processing procedures are described below. Firstly, the imbibition front positions and imbibition regions were identified and marked based on the experimental images in Fig. 3. Corresponding target pixels were extracted using the colour threshold method according to the RGB colour difference between the marked imbibition area and the background area. Secondly, pixel-physical coordinate calibration was conducted with reference to the width and length boundaries of the sample. A linear transformation function between image pixel coordinates and actual spatial positions of the imbibition front was established to obtain the precise coordinates of the liquid absorption front at diverse locations. Finally, the pixel coordinates of the imbibition front were converted into actual imbibition distances. Equidistant sampling was carried out along the sample width at an interval of 0.02 cm to obtain systematic spatial data of the imbibition front. The complete image processing workflow is presented in Fig. 8.

Fig. 9 and Fig. 10 present the evolutionary characteristics of imbibition profiles during working fluid imbibition in samples with one groove and three grooves, respectively. Different from the approximately uniform imbibition profile of the benchmark sample shown in Fig. 8(c), the imbibition profiles on both sides of the single groove remain relatively stable and smooth. This indicates that a single groove has a negligible influence on the stability of the imbibition front in mesh area. In contrast, samples with three grooves exhibit prominent fluctuations in the imbibition front profile. The superposition effect of multiple grooves severely disturbs the imbibition behavior, resulting in a significant deterioration in the stability of the imbibition front.

Table 2
Parameter values for Lucas–Washburn (L-W) theoretical prediction model.

r, effective pore size	σ, interfacial tension	θ, contact angle	μ, dynamic viscosity	τ, tortuosity
33 μm	0.0296 N/m	5	2.35×10^{-3} Pa·s	1.5, 1.6, 1.7

To quantitatively analyze the effects of grooved structures on the stability of the imbibition front, we define the front roughness index R_f, which is expressed as:

$$R_f = L_1/L_2 - 1 \quad (2)$$

Where, L_1 represents the actual length of the imbibition front contour, and L_2 represents the specimen width (4 cm). Using the same method as in Fig. 8, the imbibition front profiles at different spatiotemporal positions are obtained for all specimens. The actual contour lengths of the imbibition front at the corresponding positions are precisely measured using ImageJ, and the front roughness indices R_f are calculated accordingly. The results are summarized in Fig. 11. The results show that the plain wire mesh specimen without grooves exhibits consistently low R_f values (about 0.005–0.035), indicating that its imbibition front is approximately a flat, piston-like advancement. In contrast, the introduction of grooved structures leads to a significant increase in R_f, and the effect strongly depends on both the number and diameter of the grooves. For the same groove diameter, specimens with three grooves always yield larger R_f than those with a single groove. At the final measurement position (9 cm), the three-groove configurations achieve R_f values of 2.46 (1 mm), 1.68 (1.5 mm), and 2.97 (2 mm), which are 2.7, 2.3, and 1.4 times those of the corresponding single-groove specimens, respectively. The influence of groove diameter is more complex: for single-groove specimens, the 2 mm diameter produces the highest R_f (2.16 at 9 cm), while the 1.5 mm diameter gives the lowest (0.73); however, all grooved specimens exhibit R_f values larger than those of the groove-free specimen. Moreover, for all specimens containing grooves, R_f increases monotonically with imbibition distance, demonstrating progressive amplification of fingering instability. These quantitative results confirm that increasing the number of grooves aggravates front instability, and that the number of grooves has a stronger influence on front stability than the groove size. These findings are consistent with the results reported by others work, suggesting that the number of grooves is one of the key parameters controlling the stability of the imbibition front in composite porous media [30–32].

As shown in Fig. 12, from the perspective of imbibition development, the unstable evolution of the imbibition front can be qualitatively explained by the difference in lateral liquid supply patterns: a single groove supplies liquid to both sides simultaneously, while multiple grooves create bidirectional lateral feeding toward the central mesh region. Specifically, when only one groove is present, it must supply liquid simultaneously to the wire mesh regions on both sides, thereby dispersing its liquid supply capacity. In this case, the evolution of the imbibition front in the wire mesh regions relies primarily on their own capillary forces. When the number of grooves increases to three, as shown in Fig. 13, the left and right grooves simultaneously supply liquid to the central wire mesh region, forming a bidirectional transverse liquid supply pattern. This configuration produces an effect akin to compressing the front from both sides toward the center, thereby exacerbating the instability of the imbibition front and inducing a pronounced fingering phenomenon. Moreover, the difference in fluid transport capacity between grooves and their adjacent wire meshes triggers cross-structure fluid mass exchange, which constitutes one major source of lateral liquid replenishment [33]. Therefore, achieving a relatively ideal piston-like imbibition front requires effective control over the number of grooves.

4.3. Interfacial instability mechanisms

In the imbibition system of wire mesh with grooved structures investigated in this study, the introduction of grooves alters the micro-

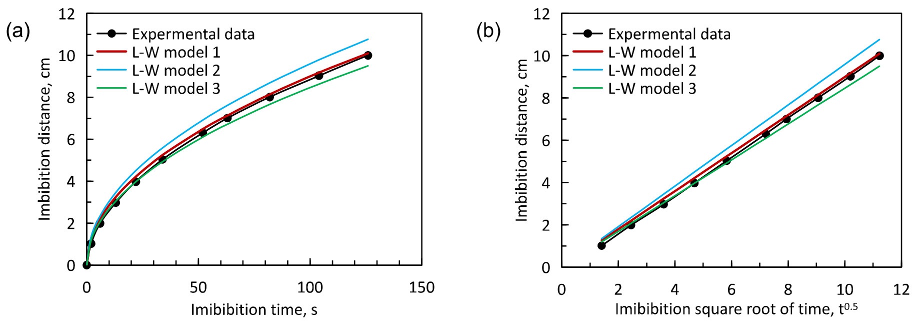

Fig. 7. Comparison curves of imbibition experimental data of wire mesh specimens and L-W theoretical predictions. Model 1, τ =1.6. Model 2, τ =1.5. Model 3, τ =1.7. (a) Imbibition distance versus imbibition time; (b) Imbibition distance versus the square root of imbibition time.

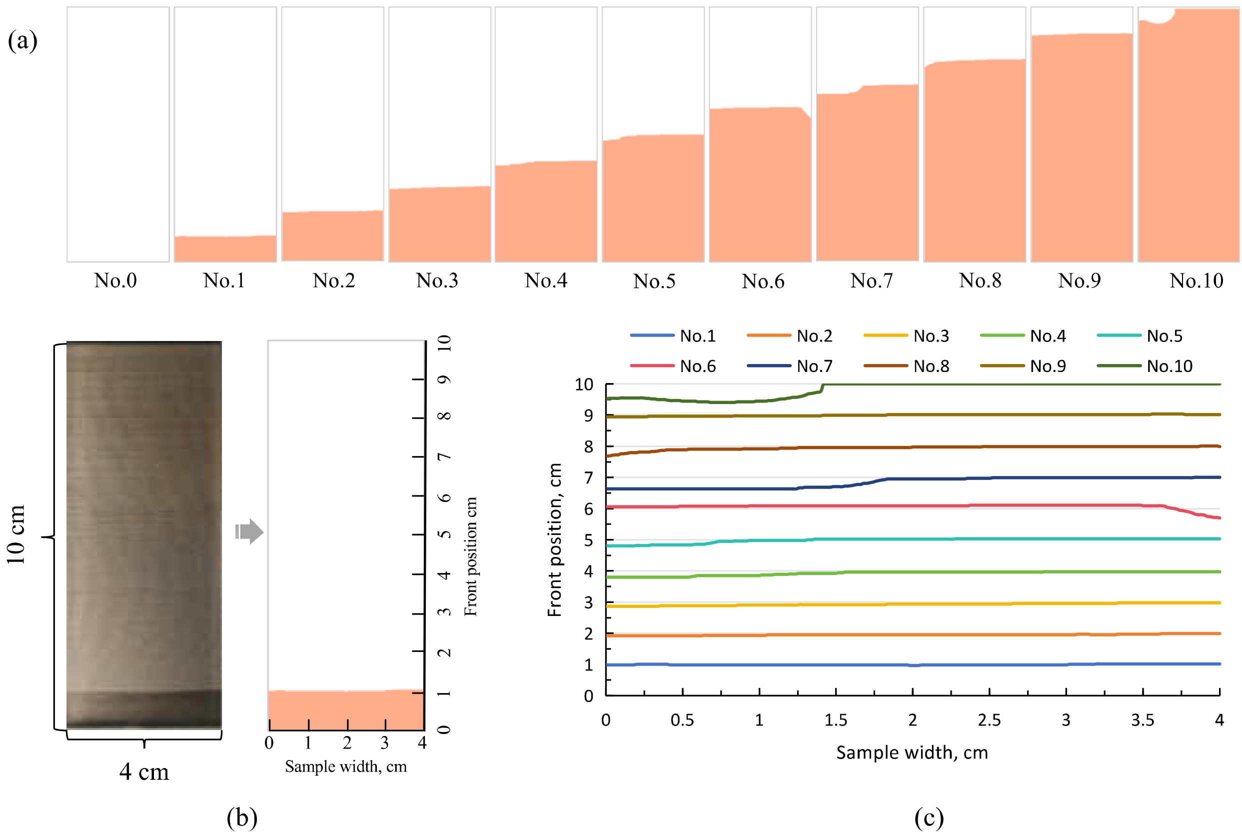

Fig. 8. Data processing procedures for imbibition profile evolution of working fluid in wire mesh samples. (a) Extraction of sequential images of imbibition profiles. (b) Coordinate calibration of imbibition positions on samples. (c) Evolution curves of imbibition profile positions.

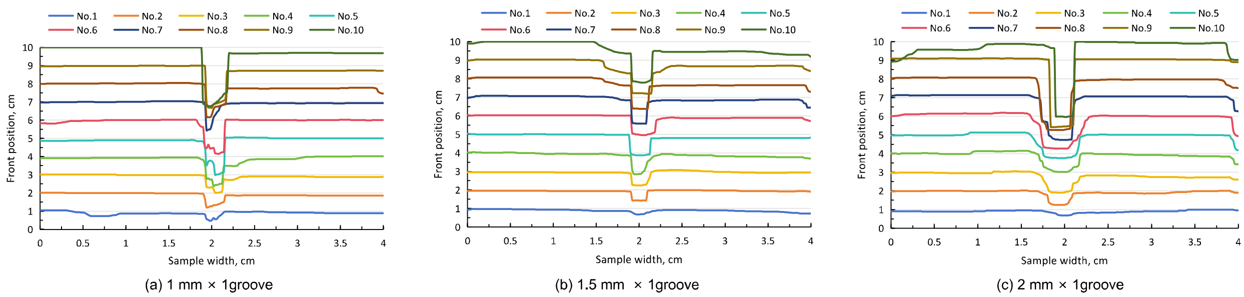

Fig. 9. Evolution of imbibition profiles for specimens with a single groove.

scopic pore structure of the wire mesh specimen, thereby influencing the morphological evolution of the imbibition front and the interfacial stability [34]. The microstructural characteristics of the wire mesh specimen containing grooved structures were examined using electron

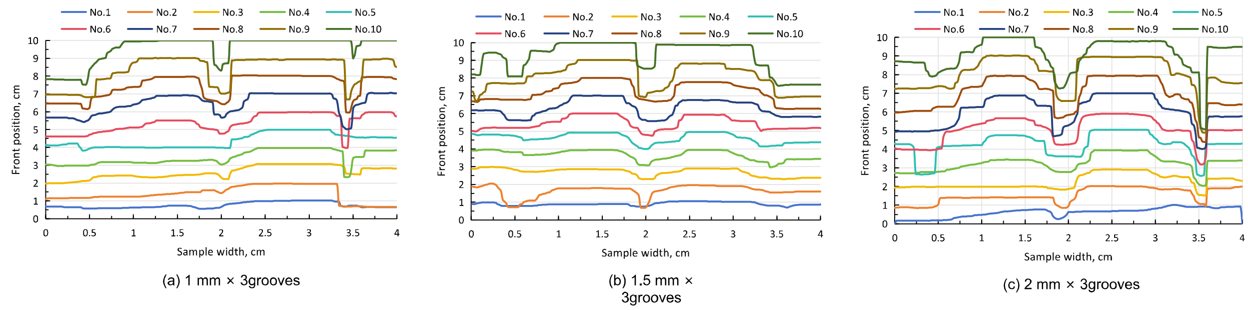

Fig. 10. Evolution of imbibition profiles for specimens with three grooves.

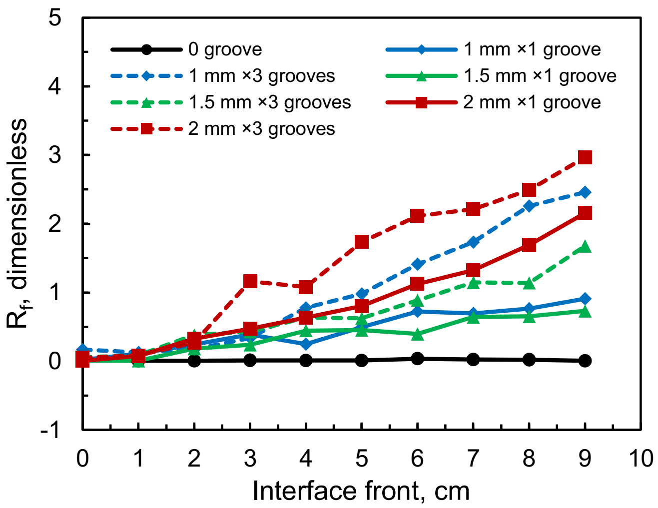

Fig. 11. Evolution of the front roughness index with imbibition distance for wire mesh specimens having different groove numbers and diameters.

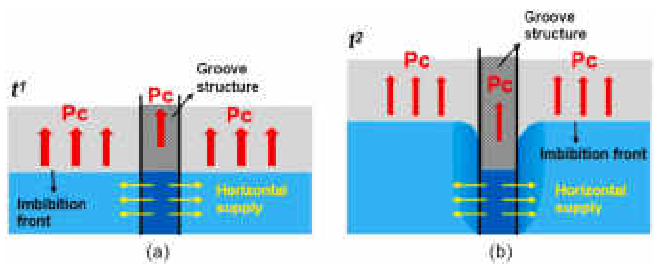

Fig. 12. Schematic diagram of the working fluid imbibition mechanism in the central wire mesh region under the condition of one grooved Structure.

microscopy, as shown in Fig. 14. In the transition zone at the interface between the groove and the wire mesh, compression reduces the effective pore diameter; in contrast, the pore structures of the groove body region and the intrinsic wire mesh region remain relatively unchanged. These modifications directly determine the distribution characteristics of the capillary pressure field. According to the Young-Laplace equation, $Pc \propto 1/r_{eff}$, consequently, the effective capillary pressure in the transition zone reaches a local maximum, thereby generating a transverse capillary pressure gradient along the specimen width. It is crucial to distinguish between the static capillary pressure (Pc) and the liquid-phase pressure (P_{liquid}) that governs actual fluid flow. According to the relation $P_{liquid} = P_{gas}$ - Pc, where P_{gas} denotes the ambient gas pressure, the severely compressed pores in the transition zone, which possess the highest capillary pressure, actually correspond to the lowest liquid pressure-a pressure valley rather than a pressure peak. This localized minimum liquid pressure serves as the fundamental driving force that draws the

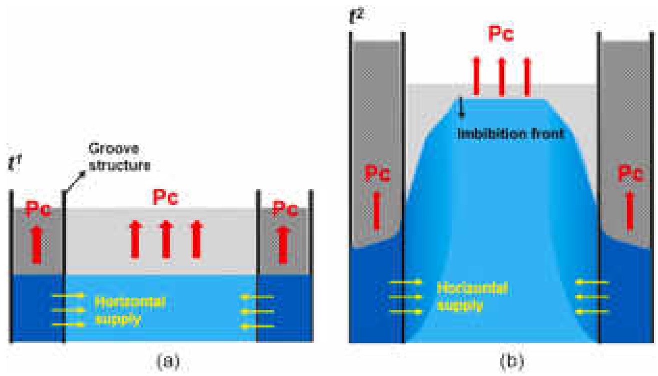

Fig. 13. Schematic diagram of the working fluid imbibition mechanism in the central wire mesh region under the condition of three grooved structures.

wetting liquid out of the grooves into the transition zone. Once this narrow zone is rapidly saturated, the local gas-liquid interface vanishes, and the capillary pressure within the transition zone drops sharply. The transition zone then functions as a liquid bridge, enabling sustained lateral flow from the groove to the adjacent mesh regions. Therefore, during spontaneous imbibition, the working fluid inside the grooves not only advances along the primary imbibition direction but is also driven by the transverse capillary pressure gradient to undergo lateral imbibition into the wire mesh regions on both sides, establishing a transverse liquid supply mechanism.

This transverse liquid supply process provides additional liquid replenishment to the imbibition front in the wire mesh regions on both sides of the grooves, significantly enhancing the local displacement velocity. Meanwhile, because the grooves continuously supply liquid to the adjacent wire mesh regions, the advancement of the working fluid front inside the grooves along the primary imbibition direction lags behind. The resulting non-uniform distribution of the normal velocity theoretically satisfies the perturbation amplification condition for immiscible two-phase displacement fronts in porous media proposed by Chuoke et al. (1959), ultimately evolving into the pronounced fingering phenomenon observed experimentally [26,35,36] Based on the Saffman-Taylor instability theory [37], Chuoke et al. (1959) established a linear stability criterion for immiscible two-phase displacement fronts in porous media. According to this criterion, whether an initial small perturbation amplifies depends on the following condition, given a transverse velocity gradient at the front:

While Chuoke's classical theory was originally derived for viscous fingering during immiscible displacement, its fundamental premise which perturbations at the interface grow when the driving pressure gradient overcomes the stabilizing capillary forces-remains applicable to our hybrid porous system. However, in our spontaneous imbibition regime, the process is capillary-dominated rather than viscous-dominated. Therefore, a modified analytical framework inspired by Chuoke's instability criterion is adopted to quantify the fingering

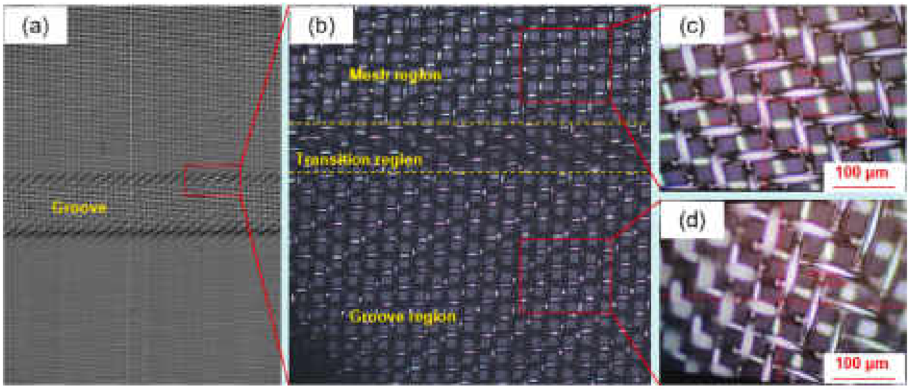

Fig. 14. SEM images of the micro structure of the wire mesh with groove. (a)-2×; (b)-5×; (c) and (d)-10×.

evolution. In this context, the lateral capillary pressure gradient between the groove and the mesh acts as the primary driving force for the perturbation growth, replacing the viscous pressure gradient in the original theory. Based on the Young-Laplace equation, the lateral capillary pressure, ΔP_c, can be approximated as:

$$\Delta P_c = P_c^{transition} - P_c^{groove} \approx 2\sigma_e\left(\frac{1}{r1} - \frac{1}{r2}\right)cos\theta \quad (2)$$

In the Eq. (2), $P_c^{transition}$ represents the capillary pressure of the transition zone; P_c^{groove} represents the capillary pressure of the groove zone; r_1 and r_2 represent the effective pore size of transition and groove zone; σ_e is the kerosene-air interfacial tension, and θ is the contact angle. This pressure difference drives the working fluid to flow laterally from the groove into the adjacent mesh regions, thereby generating a velocity gradient perpendicular to the main imbibition direction at the advancing front.

Opposing this driving action is the stabilizing effect of interfacial tension. When a small perturbation appears at the imbibition front, the curved liquid-gas interface creates an additional Laplace pressure that tends to restore a flat interface. For an interfacial deformation with a characteristic length scale β, the magnitude of the restoring pressure provided by interfacial tension is of the order σ_e/β. Therefore, the competition between the transverse capillary driving force and the stabilizing interfacial tension can be characterized by the following transverse capillary number C_{at}:

$$C_{at} = \frac{\Delta P_c}{\sigma_e/\beta} \quad (3)$$

Physically, this dimensionless number C_{at} represents the competition between the destabilizing transverse capillary force ($\Delta P_c{\cdot}\beta$) and the stabilizing force of interfacial tension (σ_e). When $C_{at} > 1$, the transverse liquid supply driven by the structural heterogeneity overcomes the interface's resistance to deformation, leading to the observed fingering instability.

It should be noted that, unlike the classical Saffman-Taylor or Chuoke viscous fingering, the driving force in the present system is not an externally applied pressure gradient but a transverse capillary pressure gradient induced by structural heterogeneity. Hence, the C_{at} defined here is an adaptive criterion for capillary-dominated spontaneous imbibition systems; it can be regarded as a variant of the transverse Bond number, measuring the relative strength of the transverse capillary drive versus the capillary stabilizing effect.

Based on the characterization results shown in Fig. 14 and the experimental parameters, C_{at} can be approximately estimated. Since the structural variations are the most drastic within the transition zone, and all instabilities of the working fluid imbibition front originate at the junctions between grooves and wire meshes, the width of the transition zone is reasonably approximated as the characteristic wavelength. The transition zone width is taken as 80 μm based on SEM results, and σ_e as the kerosene-air interfacial tension of 0.02961 N/m at a room temperature of 21 °C. The results are presented in Table 3. Assuming a reasonable contact angle θ of 15°, ΔP_c is estimated from the Young-Laplace equation to be approximately range in 4188 Pa to 4259 Pa, and the final calculated values of C_{at} are in the ranges of 11.32–11.50, much bigger than 1, indicating that the interface becomes unstable and will develop into fingering. This theoretical result is consistent with the fingering phenomenon observed in the experiments, demonstrating that the grooved structures induces a significant transverse velocity gradient by reconstructing the transverse capillary pressure field, thereby triggering the instability of the imbibition front and the development of fingering.

Furthermore, the C_{at} criterion can reasonably explain the effect of the number of grooves on front stability. When the number of grooves increases, the mesh region between adjacent grooves receives lateral liquid supply from both sides (as illustrated in Fig. 13). This superposition of transverse capillary driving effectively increases the local ΔP_c, thereby raising C_{at} and intensifying fingering. This explains why the three-groove specimens exhibit a more pronounced non-uniform interface than the single-groove specimens in the experiments.

4.4. Imbibition rate of mesh and groove area

When grooved structures are introduced, the imbibition front of the working fluid inside the wire mesh specimen is no longer characterized by uniform piston-like advancement. An imbibition velocity difference in the evolution of the imbibition interface emerges between the grooves and the adjacent wire mesh regions, manifested by the fact that the imbibition front in the wire mesh regions consistently advances faster than that inside the grooves. Therefore, to quantitatively analyze this velocity difference, the farthest imbibition front (corresponding to the wire mesh regions) and the shortest imbibition front (corresponding to the grooves) at the same time instant were selected for analysis. First, all experimental specimens were classified into three categories: specimen without groove, specimen containing one single groove, and specimen fitted with three grooves. Next, to account for the symmetry of spatial configurations, the schematic diagram in Fig. 15 was adopted to partition the groove structures and wire mesh regions to yield seven distinct research subjects. Subsequently, quantitative characterizations were

Table 3
The calculation result of C_{at} of the specimen with different groove sizes.

Groove size, mm	σ_e, N/m	β, μm	r_1, μm	r_2, mm	θ, °	C_{at}, dimensionless
1				0.5		11.32
1.5	0.02961	80	10	0.75	15	11.68
2				1		11.50

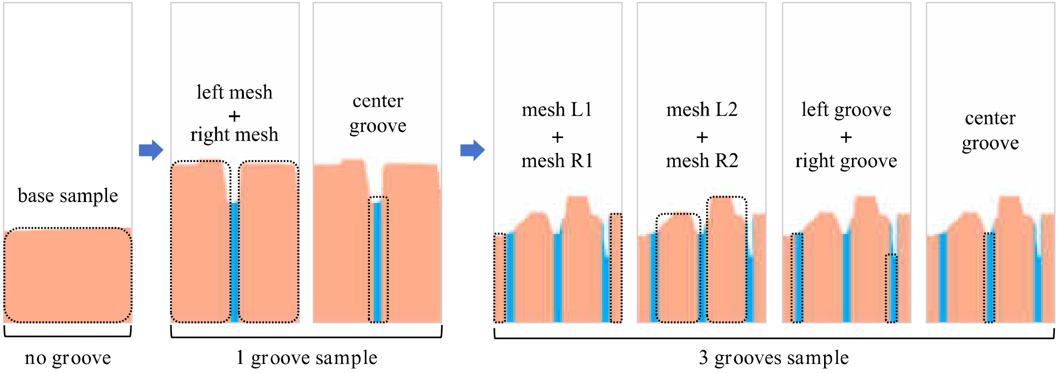

Fig. 15. Schematic diagram of the categorized mesh and groove regions for various specimen configurations. The orange regions denote wire mesh domains, cyan areas correspond to grooved flow channels, and black dashed lines mark identical structural features. (For interpretation of the references to colour in this figure legend, the reader is referred to the web version of this article.)

carried out for each subject to quantify how imbibition distance of the working fluid evolves over time. During quantification, the maximum advancing distance of the imbibition front was adopted as the sampling criterion: data points were recorded once the working fluid advanced 1 cm within the mesh region, with the corresponding imbibition time logged and the concurrent interfacial imbibition propagation distance inside the groove structure measured synchronously. Finally, relational curves of working fluid imbibition distance versus time were plotted separately for the groove structures and wire mesh regions across all specimens based on the collated statistical datasets.

Spontaneous imbibition curves measured from groove-free mesh samples were used as the baseline reference to comparatively investigate the imbibition behaviors within mesh domains and groove interiors under different groove configurations. The introduction of grooves consistently accelerates liquid uptake in adjacent mesh regions relative to the groove-free benchmark, regardless of groove number (Figs. 16 and 17). For single-groove specimens, the mesh regions on both sides of the groove exhibit nearly identical imbibition curves, confirming that a single groove exerts negligible disturbance on front symmetry (Fig. 16). In three-groove specimens, however, the central mesh region-flanked by two grooves-shows a distinctly faster imbibition rate than the outermost mesh strips, which are influenced by only one groove (Fig. 17). This spatial disparity arises from the superposition of transverse capillary supply from both sides.

Inside the grooves themselves, the axial imbibition velocity is consistently lower than that in adjacent mesh zones throughout the early and intermediate stages, because grooves continuously divert liquid laterally to feed the surrounding meshes (Figs. 18 and 19). Nevertheless, a notable difference exists between single- and triple-groove configurations: the single groove exhibits an imbibition rate even lower than the groove-free benchmark, whereas all grooves in the triple-groove specimen surpass the benchmark rate. This is because the liquid supply burden per groove is substantially alleviated when multiple grooves share the task of feeding the mesh regions (Fig. 19). In the late stage, once the adjacent meshes approach full saturation, lateral diversion ceases and the axial velocity inside grooves rises sharply, as seen in the upward inflection of the corresponding curves (Figs. 18 and 19).

We further calculate the longitudinal transient imbibition velocity of the working fluid in groove and wire mesh regions. The velocity is determined by the following formula: $\upsilon = (d_{i+1} - d_i)/(t_{i+1} - t_i)$, where d denotes the imbibition distance (cm) and t denotes the corresponding imbibition time (s). Notably, for samples with three grooves, the imbibition boundaries of the outermost meshes and edge grooves differ significantly from those of the central groove and intermediate meshes. Therefore, only the central groove and its adjacent mesh regions are selected for statistical analysis of local transient imbibition velocity. The corresponding velocity variation curves for different groove structures and mesh regions are presented in Fig. 20. It can be concluded that the incorporation of groove structures effectively elevates the transient imbibition velocity within mesh regions. In addition, the transient velocity in groove regions increases remarkably during the late imbibition period, which is in good agreement with the previously analyzed imbibition characteristics and experimental phenomena.

5. Conclusions

This study fabricated 400-mesh metal wire mesh specimens with varying groove configurations and high-spatiotemporal-resolution visualization experiments were conducted to reveal how grooves regulate horizontal spontaneous imbibition of working fluid within dual-scale wire-mesh porous media. The core findings are summarized as follows:

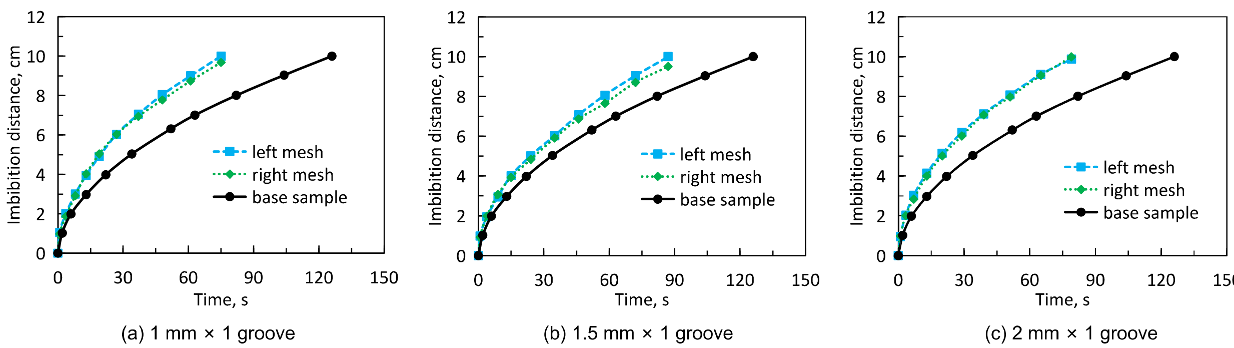

Fig. 16. Comparison of imbibition curves for different wire mesh regions in single-groove specimens against the benchmark sample.

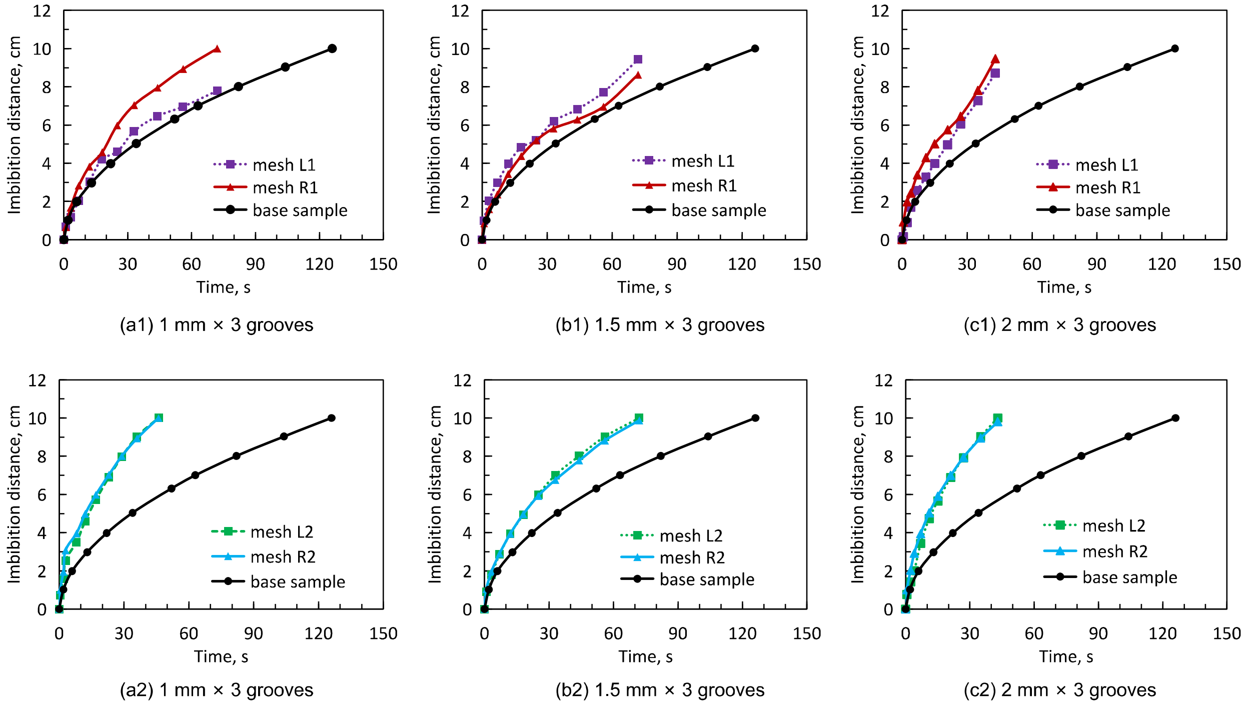

Fig. 17. Comparison of imbibition curves for different wire mesh regions in three-groove specimens against the benchmark sample.

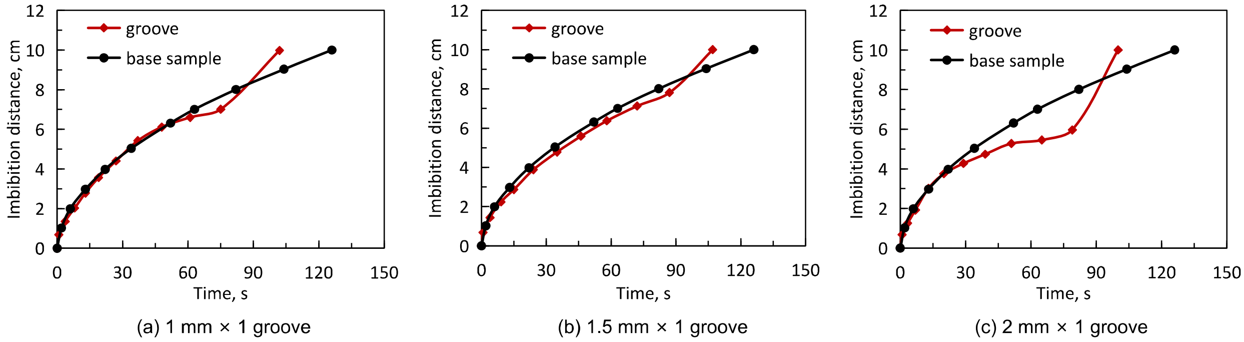

Fig. 18. Comparison of imbibition curves for groove region in single-groove specimens against the benchmark sample.

(1) Groove-free meshes exhibit stable piston-like imbibition that follows the Lucas-Washburn model. Grooves induce transverse liquid replenishment to adjacent meshes, accelerating mesh imbibition but destabilizing the overall liquid front.

(2) Single-groove structures boost mesh imbibition speed while retaining stable piston-like front propagation on both sides of the groove. In multi-groove layouts, adjacent grooves deliver liquid to the central mesh area; superimposed transverse capillary driving forces concentrate in this central zone and trigger severe fingering instability, which becomes more pronounced as groove diameter increases.

(3) The imbibition rate is governed primarily by groove count rather than groove cross-sectional dimension. With identical groove dimensions, mesh regions surrounded by multiple grooves deliver notably faster imbibition relative to those adjacent to a single groove. At a fixed groove number, adjusting groove diameter only yields marginal improvement in liquid uptake speed. In the early and intermediate imbibition phases, grooves continuously feed liquid sideways into surrounding meshes, which restrains their own axial imbibition and keeps their internal flow velocity below that of nearby mesh zones. After lateral liquid replenishment fades away, the imbibition velocity within grooves rises distinctly in the late-stage imbibition process.

(4) Future work can further explore how groove cross-sectional shapes, layout arrangements and coupled geometric parameters alter imbibition characteristics. Combined in-situ microscopic observation and numerical simulation will help clarify the mass transfer interaction between grooves and wire meshes. Such efforts can inform structural design methods that balance imbibition front stability and liquid transport efficiency for dual-scale porous wick materials.

CRediT authorship contribution statement

Jian Tian: Writing – original draft, Investigation, Funding acquisition, Formal analysis, Conceptualization. **Yugao Ma:** Supervision, Resources, Project administration, Funding acquisition. **Haonan Hou:** Visualization, Investigation, Formal analysis, Data curation. **Suyi Zhang:** Validation, Formal analysis. **Chaozhong Qin:** Writing – review & editing, Supervision, Methodology, Conceptualization.

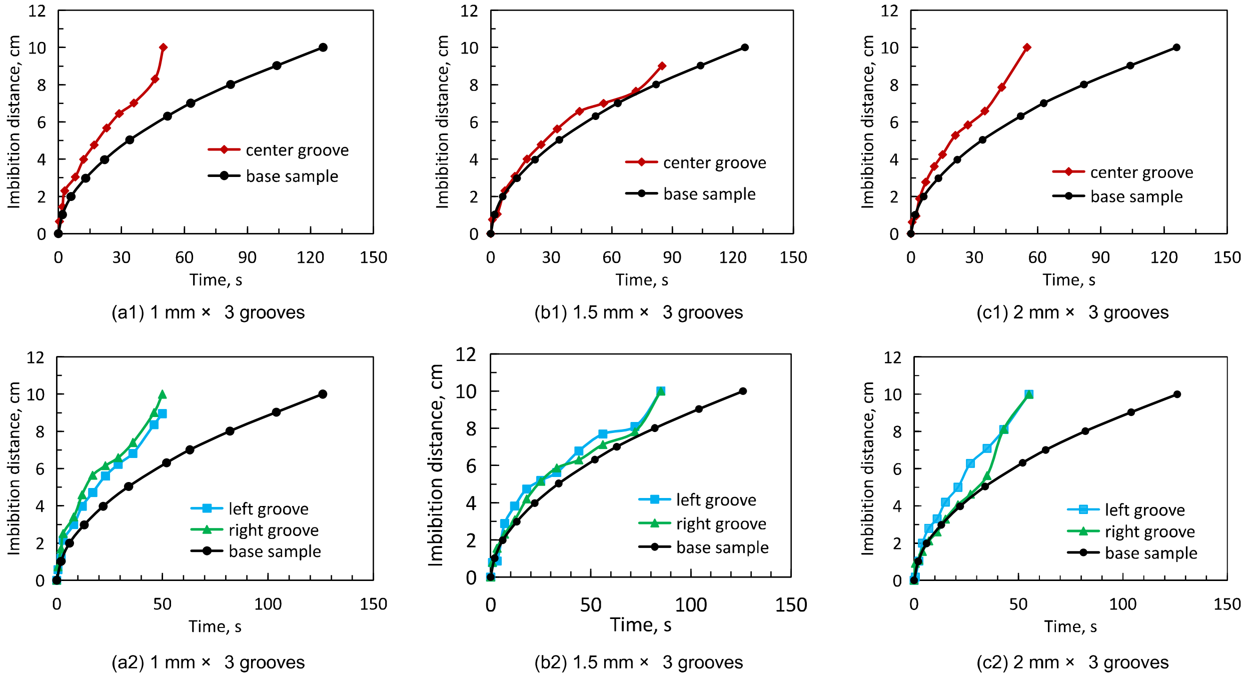

Fig. 19. Comparison of imbibition curves for different groove regions in three-groove specimens against the benchmark sample.

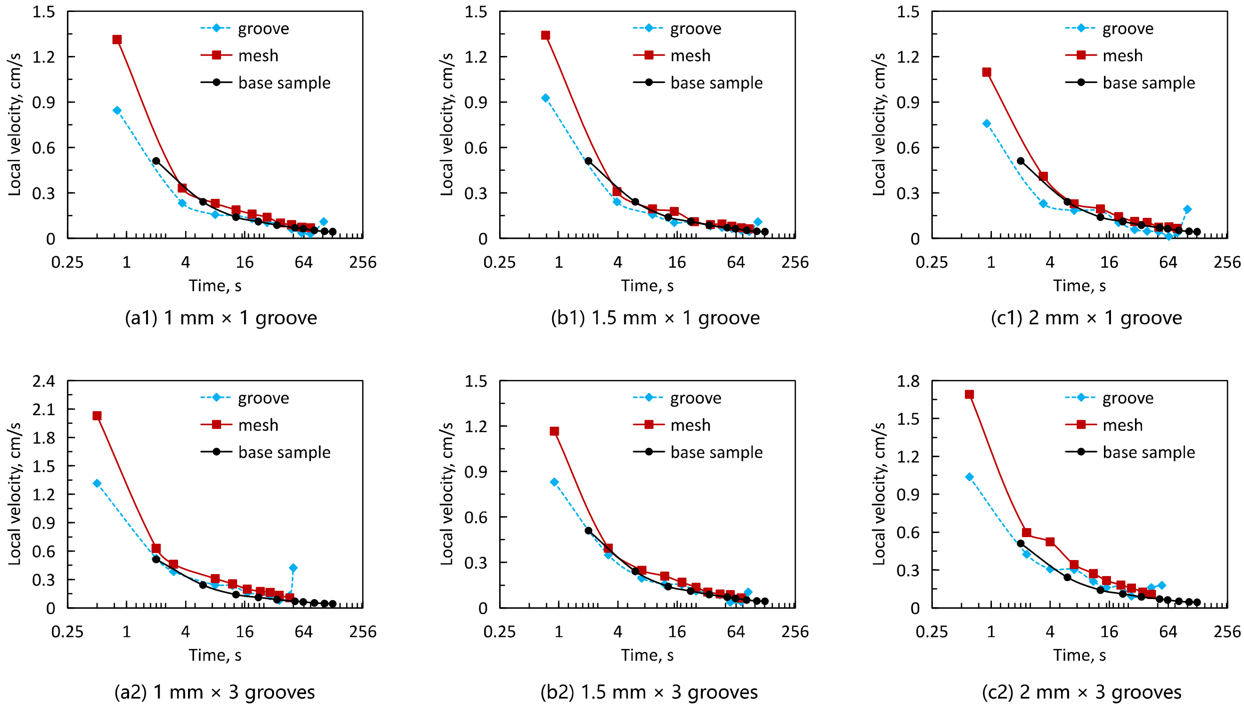

Fig. 20. Comparison of transient imbibition velocity curves among distinct wire mesh zones, groove zones and the benchmark sample.

Declaration of competing interest

The authors declare no competing interest.

Acknowledgments

This work was financially supported by the National Natural Science Foundation of China (Grant No. 52404023), the Stable Support Scientific Research Project of R&D Platform of China National Nuclear Corporation (WDZC-2024-CXZX07), and the General Program of the Natural Science Foundation of Chongqing (Grant No. CSTB2025NSCQ-GPX0712).

Data availability

Data will be made available on request.

References

[1] J.C. Cai, Y. Chen, Y. Liu, et al., Capillary imbibition and flow of wetting liquid in irregular capillaries: a 100-year review, Adv. Colloid Interf. Sci. 302 (2022) 102654.

[2] P.L. Wang, J. Gao, B.Q. Xiao, et al., The fastest capillary flow in root-like networks under gravity, Langmuir 48 (18) (2024) 9741–9750.

[3] Y.B. Shao, L.F. Xu, J.Q. Li, et al., Polymer electrolyte membrane fuel cell transient voltage characteristic considering liquid water imbibition and drainage in gas diffusion layer, J. Power Sources 493 (2021) 229683.

[4] C. Noe, S. Morankar, A.S. Rattner, et al., Structured, sintered, and rastered strategies for fluid wicking in additively manufactured heat pipes, Addit. Manuf. 99 (2025) 104669.

[5] A.E. Essien, S.E. Dickson-Anderson, Y.P. Guo, Microplastics and nanoplastics in stormwater management engineered porous media systems: a systematic review of their sources, transport, retention, and removal characteristics, Environ. Sci. Adv. 27 (2025) 215–238.

[6] M. Holz, M. Zarebanadkouki, P. Benard, Root and rhizosphere traits for enhanced water and nutrients uptake efficiency in dynamic environments, Front. Plant Sci. 15 (2024) 1415678.

[7] X.Y. Jia, J. Yang, M. Lin, et al., Pore scale analysis for flow and thermal characteristics in metallic woven mesh, Int. J. Heat Mass Transf. 218 (2024) 124740.

[8] Y.G. Ma, H.X. Yu, X.Q. Wang, et al., Experimental study on sodium screen-wick heat pipe capillary limit, Appl. Therm. Eng. 227 (2023) 120397.

[9] Y.Y. Fu, D. Chen, Y.X. Cui, et al., Numerical investigation of the screen mesh effects on the heat transfer performance of wick structured heat pipe, Ann. Nucl. Energy 223 (2025) 111655.

[10] Q. Chen, J.W. Li, T.S. Cong, Research on heat transfer performance of spiral woven wire mesh composite capillary wick ultra-thin heat pipe, Appl. Therm. Eng. 262 (2024) 125261.

[11] P. Vishwakarma, J. Punch, E. Guinan, et al., A systematic review of composite wick designs for enhancing capillary and thermal performance in heat pipes, Int. J. Heat Mass Transf. 235 (2025) 126401.

[12] S.C. Tan, X.B. Pang, Q. Xu, et al., Study on the permeability and capillary pressure of spiral woven mesh for flat-plate heat pipes, Appl. Therm. Eng. 256 (2024) 124118.

[13] J.C. Tang, X.G. Hu, Evaluation of capillary wetting performance of micro-nano hybrid structures for open microgrooves heat sink, Exp. Thermal Fluid Sci. 112 (2020) 109948.

[14] S.C. Wong, M.S. Deng, Performance tests on triple composite mesh-groove-powder wicks in a visualizable flat-plate heat pipe, Int. J. Heat Mass Transf. 219 (2024) 124912.

[15] H.D. He, J.P. Li, Z.Y. He, et al., Preparation of hierarchical microgroove textures on the surface of Al-based wicks by roller pressing and laser scanning irradiation, Surf. Coat. Technol. 487 (2024) 131008.

[16] G.R. Abdizadeh, S. Noori, M. Saeedi, A robust three-dimensional numerical model for heat transfer characteristics in sintered-grooved thin flat heat pipes, Phys. Fluids 36 (7) (2024) 073608.

[17] C. Yan, F. Lu, G. Chen, et al., Fabrication and capillary performance of microgroove wick structures for ceramic vapor chambers, Int. Commun. Heat Mass Transfer 172 (1) (2026) 110264.

[18] D. Khrustalev, A. Faghri, Coupled liquid and vapor flow in miniature passages with microgrooves, J. Heat Transf. 121 (3) (1999) 729–733.

[19] S. Ravi, R. Dharmarajan, S. Moghaddam, Physics of fluid transport in hybrid biporous capillary wicking microstructures, Langmuir 32 (33) (2016) 8289–8297.

[20] G.C. Jiang, Z. Tian, X. Luo, et al., Ultrathin aluminum wick with dual-scale microgrooves for enhanced capillary performance, Int. J. Heat Mass Transf. 189 (2022) 122679.

[21] S.C. Wong, M.S. Deng, M.C. Liu, Characterization of composite mesh-groove wick and its performance in a visualizable flat-plate heat pipe, Int. J. Heat Mass Transf. 183 (Pt A) (2021) 122161.

[22] Y.M. Liu, X.L. Yang, X. Tian, et al., Capillary-driven boiling heat transfer on superwetting microgrooves, ACS Omega 7 (39) (2022) 35339–35350.

[23] M.A.F. Zarandi, K.M. Pillai, A.M.R. Hasan, Investigating liquid-fronts during spontaneous imbibition of liquids in industrial wicks: part II: validation by DNS, AICHE J. 152 (2022) 104082.

[24] R.R. Rye, F.G. Yost, J.A. Mann, Wetting kinetics in surface capillary grooves, Langmuir 12 (20) (1996) 4625–4627.

[25] K. Baraya, J.A. Weibel, S.V. Garimella, A transient heat pipe model considering wick saturation effects that predicts dynamic evaporator dryout and recovery, Int. J. Heat Mass Transf. 242 (2025) 126837.

[26] R.L. Chuoke, P. Vanmeurs, C. Vanderpoel, The instability of slow, immiscible, viscous liquid-liquid displacements in permeable media, Trans. AIME 216 (1959) 188–194.

[27] R. Lucas, Rate of capillary ascension of liquids, Kolloid-Zeitschrift 23 (1918) 15–22.

[28] E.W. Washburn, The dynamics of capillary flow, Phys. Rev. 17 (3) (1921) 273–283.

[29] Cai Jianchao, Yu Boming, A discussion of the effect of tortuosity on the capillary imbibition in porous media, Transp. Porous Media 89 (2011) 251–263.

[30] M. Chavhan, P.K. Singh, Enhancing heat pipe performance through hybrid wick structures: balancing pore size and permeability, Appl. Therm. Eng. 256 (2024) 124079.

[31] Y. Tang, D.X. Deng, G.H. Huang, et al., Effect of fabrication parameters on capillary performance of composite wicks for two-phase heat transfer devices, Energy Convers. Manag. 66 (2013) 66–76.

[32] B. Rallabandi, S. Modha, B. Kalish, et al., Wicking in paper-based devices with engineered surface grooves, Langmuir 41 (2025) 34292–34298.

[33] Y.H. Liu, B.Q. Xiao, L. Chen, et al., Monte Carlo simulation of apparent permeability for shale gas flow in three-dimensional fractal porous media, Int. Commun. Heat Mass Transfer 171 (2026) 110102.

[34] L. Maier, L. Pauly, J.T. Gostick, et al., Spontaneous imbibition in thin anisotropic fibrous media: experiments and numerical modeling, Text. Res. J. 95 (9–10) (2025) 937–955.

[35] Y. Li, G. Mason, N.R. Morrow, et al., Capillary pressure at the imbibition front during water-oil counter-current spontaneous imbibition, Transp. Porous Media 77 (3) (2009) 475–487.

[36] S.D. Gowen, T.E. Videbæk, S.R. Nagel, Measurement of pressure gradients near the interface in the viscous fingering instability, Phys. Rev. Fluids 9 (5) (2024) 053902.

[37] P.G. Saffman, G. Taylor, The penetration of a fluid into a porous medium or Hele-Shaw cell containing a more viscous liquid, Proc. R. Soc. Lond. A Math. Phys. Sci. 245 (1242) (1958) 312–329.